Twelve inequivalent Dirac cones in two-dimensional ZrB_{2}

Alejandro Lopez-Bezanilla

Phys. Rev. Materials **2**, 011002 — Published 29 January 2018

DOI: 10.1103/PhysRevMaterials.2.011002

Twelve Inequivalent Dirac Cones in Two-Dimensional ZrB_2

Alejandro Lopez-Bezanilla[1*]
Theoretical Division, Los Alamos National Laboratory, Los Alamos, NM 87545, United States and
Materials Science Division, Argonne National Laboratory,
9700 S. Cass Avenue, Lemont, Illinois, 60439, United States
(Dated: December 11, 2017)

Theoretical evidence of the existence of 12 inequivalent Dirac cones at the vicinity of the Fermi energy in monolayered ZrB_2 is presented. Two-dimensional ZrB_2 is a mechanically stable d- and p-orbital compound exhibiting a unique electronic structure with two Dirac cones out of high-symmetry points in the irreducible Brillouin zone with a small electron-pocket compensation. First-principles calculations demonstrate that while one of the cones is insensitive to lattice expansion, the second cone vanishes for small perturbation of the vertical Zr position. Internal symmetry breaking with external physical stimuli, along with the relativistic effect of SOC, is able to remove selectively the Dirac cones. A rational explanation in terms of d- and p-orbital mixing is provided to elucidate the origin of the infrequent amount of Dirac cones in a flat structure. The versatility of transition metal d-orbitals combined with the honeycomb lattice provided by the B atoms yields novel features never observed in a two-dimensional material.

I. INTRODUCTION

In the search of the materials of tomorrow's technology, graphene was considered early on as a promising candidate for development and innovation[1]. The combination of an electronic band structure hosting the so-called massless Dirac fermions, together with a weak spin-orbit coupling (SOC), enable electrons to travel at relativistic speed over very long distances at room temperature. Governed by the Dirac equation, Dirac fermions emerge at isolated points in the irreducible Brillouin zone (iBZ), where an upper band touches a lower one. In undoped graphene, two Dirac cones are centered around the two non-equivalent K and K' points with a perfect electron-hole symmetry at the Fermi level. Each Dirac cone is therefore three-fold degenerate since they are shared by three contiguous BZ, namely a BZ contains the equivalent to two inequivalent cones.

Experimental results confirmed the ability of other two-dimensional (2D) group IV materials (silicene[2,3], germanene[4,5], stanene[6]) for hosting Dirac states, and theoretical predictions suggested new compounds with similar properties (graphynes[7], 8-pmmn borophene[8]). In most cases, 2D honeycombed lattices with Dirac cones are composed of a single type of element. Although binary compositions usually yield gapped electronic structures (BN[9], MoS_2[10]), branching away from the single-element material and search for multi-atom compounds may yield similar benefits at an effective control cost.

More recently, the fabrication of a diverse array of 2D B monolayers has captivated a growing community of scientific experts focusing on their large list of exceptional physical properties[11,12]. B-based materials with additional electron-rich elements are potential candidates to expand the number of compounds with similar properties to the group IV materials. The discovery of high T_c superconductivity in MgB_2[13] caused an immediate interest to find B-based superconductors. The viability of this compound, similar to other planar diborides[14] such as B_2O and B_2Be, relies in that it is unsymmetrical isoelectronic to C, with four valence electrons per atom in average. B-based compounds analog to group IV can be extended to larger principal quantum number elements to include the richness of d-orbitals. Thus, first-principles calculations predicted the existence of massless fermions in monolayered TiB_2[15]. Polymers containing both boron and transition metals atoms have been prepared, proving a high degree of delocalization via boron and metal atoms[16].

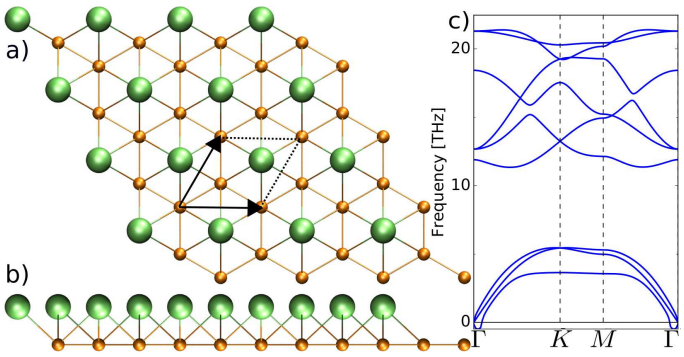

FIG. 1. Top a) and side view of a ball-and-stick representation of the hexagonal cell of monolayered ZrB_2. Zr atoms sit on the center of the hexagons of the small B atom honeycomb lattice . The hexagonal unit cell containing two atoms of B and one atom of Zr is shown in a). c) Phonon spectrum of monolayered ZrB_2

In this paper the potential scope of diborides is expanded by describing the electronic properties of metal diboride monolayered ZrB_2. Free-standing ZrB_2 is triangular borophene with Zr atoms in substitutional doping, and is predicted to exhibit 12 non-degenerate Dirac cones in the vicinity of Fermi level with a small compensated electron-hole pocket. This material features an infrequent property in a hexagonal lattice such as the displacement of the Dirac cones to lines joining two high-symmetry points of the iBZ. Both hexagonal β-graphyne[7]

and TiB_2[15] have been reported to exhibit six low symmetry Dirac points in the first BZ, and the use of Rashba SOC has been proposed[17] for splitting them into 12. Instead of resorting to the spin degree of freedom, we propose the interplay of p and d orbitals to generate six groups of two inequivalent Dirac points in the low energy spectrum of a P6mm space group material. Zr atom d-orbitals yield the formation of the Dirac cones with some contribution from the B p_z orbitals.

Contrary to the current trend of identifying new materials with improved functionalities by means of high-throughput screening of thousands of compounds, here we present a one-at-a-time material study to provide a detailed analysis of a nanostructure designed upon examination of the physico-chemical properties of its constituents.

II. COMPUTATIONAL METHODS

Calculations were performed with the `SIESTA` code. A double-ζ polarized basis set was used and the radial extension of the orbitals had a finite range with a kinetic energy cutoff of 50 meV. Electron exchange and correlation was described within the Perdew, Burke, and Ernzerhof[18] scheme of the generalized gradient approximation. The integration in the k-space was performed using a 64×64×1 Monkhorst-Pack[19] k-point mesh centered at Γ-point. To determine accurately the location of the Fermi level, a set of 320×320×1 k-points were used in a single-energy point calculation. Lattice constants and atomic coordinates were fully relaxed until the residual forces were smaller than 10^{-3} eV/Å. Phonon diagram dispersion was calculated with the `PHONOPY` code[20] using the force-constant method. Single-energy point SOC calculations were carried out with `Elk` code[21] with similar parameters.

III. RESULTS AND DISCUSSION

In 2D ZrB_2, the honeycomb lattice of B atoms exhibits a B-B distance of 1.85Å, and the Zr atoms sit over the hexagon hole at 1.48Å (see Figure 1). The lattice parameter is 3.17Å. With its vacant p_z orbital, three-fold coordinated B is an electron deficient atom and a strong p-electron acceptor. It is worth noting that vertical AA stacking of single hexagonal layers yields bulk ZrB_2, a ceramic material with a hexagonal covalent structure possessing good thermal and electrical conductivities. The crystal structure belongs to the space group P6/mmm, where the Zr atoms sit in between two hexagons of two parallel B honeycombed latticesices. Temperature dependent resistivity and high frequency susceptibility measurements in ZrB_2 revealed a superconducting transition at 5.5 K[22]. Thin films of ZrB_2 can be grown by chemical vapour epitaxy on Si wafers, to additionally provide an electrically conductive substrate for GaN[23], or the synthesis of monolayered materials[24].

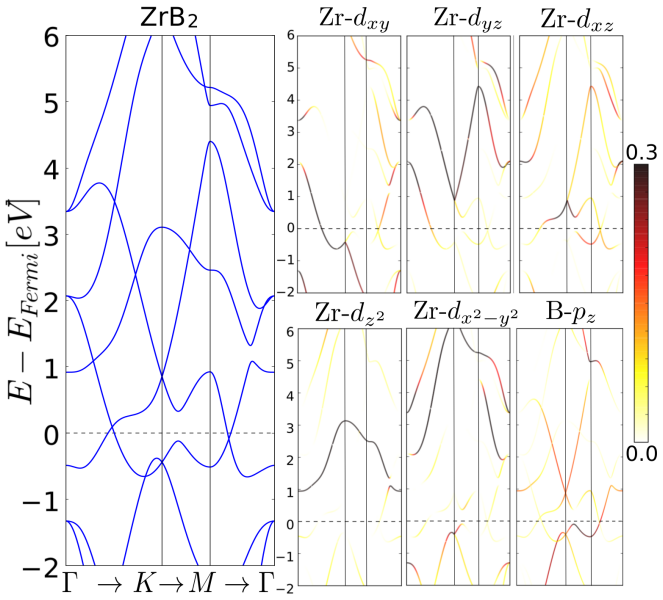

FIG. 2. Left panel: Electronic band diagram in the irreducible Brillouin zone of free-standing monolayered ZrB_2. Right panels: color-resolved projected density of states onto each Zr d-orbitals and B p_z orbital.

Isolating a single layer reduces the symmetry to P6/mm, and the BZ of interest is the area delimited by the Γ, M, and K points in the hexagonal reciprocal lattice. The monolayer (see unit cell in Figure 1b) is dynamically stable as verified by the absence of negative frequencies in the phonon spectrum shown in Figure 1c. Only one of the acoustic modes undergoes a tiny deviation towards negative frequencies close to the Γ point. 9 modes are extended over a frequency range of ∼21 THz. The in-plane acoustic branches are characterized by linear dispersions at low momentum near the center of the BZ. The out-of-plane phonon branches exhibit non-linear energy dispersions at the zone edge. While most acoustic modes exhibit ∼6 eV dispersive branches in the lower quarter of the spectrum, a frequency gap separates optical modes in the upper half, which are equally dispersive spanning altogether a range of ∼10 THz.

The band structure of the hexagonal 2D lattice is displayed in the left panel of Figure 2. Two bands form a Dirac cone in the $\Gamma - K$ line slightly above the Fermi level creating a small electron pocket. To compensate the lack of electrons, a similar hole pocket is formed upon two bands creating a second Dirac cone slightly below the Fermi energy level in the $M - \Gamma$ line.

In the hexagonal pyramid configuration, monolayered ZrB_2 belong to the C_{6v} point group. According to this symmetry representation, the five Zr d-orbitals are grouped in three groups, where two in-plane orbitals are degenerate (e_2), two out-of-plane orbitals also form a degenerate pair (e_1), and d_{z^2} remains non-degenerate (a_1). To corroborate this picture and elucidate the origin of

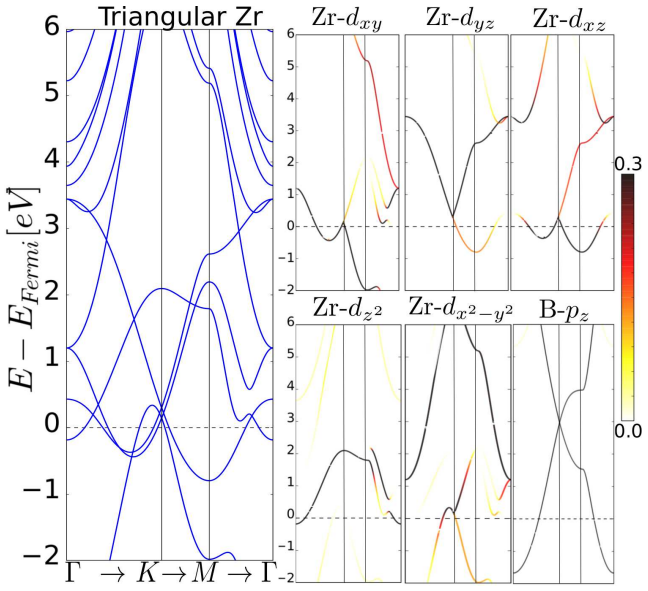

FIG. 3. Left panel: Electronic band diagram of the triangular lattice composed of uniquely the Zr atoms of the ZrB_2 lattice at fixed positions. Color-resolved panels correspond to the projected density of states of the d-orbitals, and allow to analyze the contribution of the d-orbitals separately to each electronic state. Also the p_z orbital of B atoms in an all-B honeycomb lattice is shown.

each Dirac cone, we resort to color-resolved projected density of state (PDoS) diagrams, which allow to visualize the independent contribution of each atomic orbital to the electronic states. At K point two band-crossing occur with a difference in energy of 1.29 eV. In the valence band, the d_{xy} and the $d_{x^2-y^2}$ orbitals intersect in a two-fold degenerate point (e_2), while a Dirac cone at 0.87 eV in the conduction band is created upon the d_{yz} and the d_{xz} Zr orbitals meet in a degenerate pair (e_1). The d_z^2 orbital stands alone at 3.13 eV (a_1). Note that the intensity of the lines depends on the contribution but also on the normalization factor and, although some states may appear weakly represented, the presence with light colors at the Fermi level guarantees their contribution to the Dirac cones.

The PDoS show evidence that the $\Gamma - K$ Dirac cone at the Fermi energy is created predominantly by the combination of Zr d-orbitals, whereas in the $M - \Gamma$ cone B p_z orbitals have a greater contribution. The former derives from the d_{xy}, d_{xz}, and d_{yz} orbitals, while the latter is mainly composed of d_{xz} and d_{yz} states hybridized with the B atom p_z orbital. A reminiscence of the boron honeycomb lattice is evident in the contribution of the B p_z orbitals to the Dirac cone at the K point located at ∼0.9 eV, in whose formation the d_{yz} for the upper cone and the d_{xz} for the lower one also participate. The two d_{z^2} and $d_{x^2-y^2}$ orbitals form anti-bonding states at high energy levels and do not contribute in any case to the formation of any Dirac cone. However, and as discussed below in more detail, although B atoms are crucial in the formation of the Dirac points, each cone presents different sensitivity to hybridization changes.

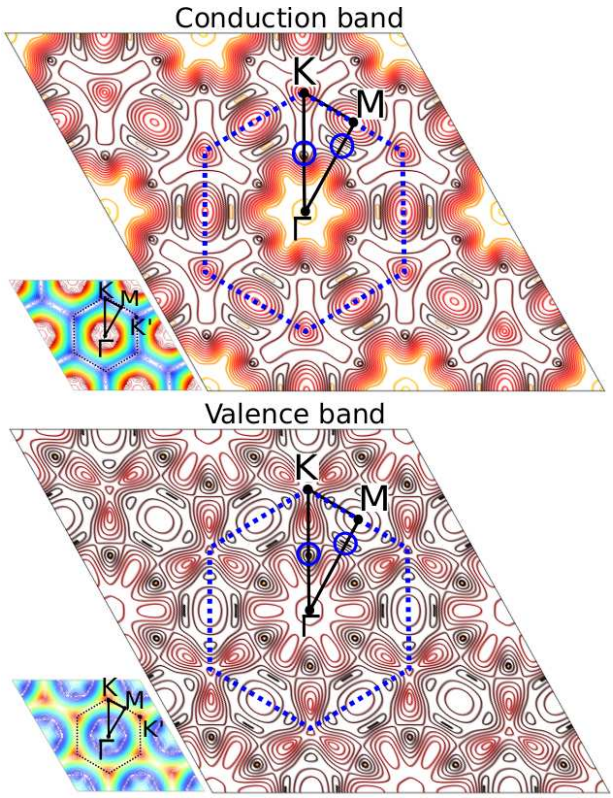

FIG. 4. Constant-energy contour plots of the conduction and valence bands of ZrB_2 in the first (enclosed by dashed hexagon) and neighbouring Brillouin zones (BZ). Smaller plots correspond to the same type of diagram of graphene electronic bands. Γ, M, and K points delimit the irreducible BZ. Circles point out the location of the ZrB_2 Dirac points. By applying the C_{6v} group symmetry operations, a total of 12 Dirac cones are obtained, in contrast to the three groups of two obtained in graphene at K and K' points.

To further support this picture of d- and p-hybridized derived Dirac states, the band diagram of the triangular lattice formed uniquely by Zr atoms at fixed positions, and with all B atoms removed, is plotted in Figure 3. A single panel showing the band developed by the lateral superposition of B atom p_z orbitals with no Zr atoms sitting on the hexagons is included. Interestingly, bands are shifted in energy and conserve the main features of the complete lattice, except the Dirac cones at the high-symmetry lines. The same group of four bands crossing at the K point are distinguishable although within a much reduced energy range of 0.16 eV.

In the $M - \Gamma$ line, the band intersection observed at 0.17 eV is composed of the d_{xz} orbital for the running up band, and of the d_{xy} and d_{z^2} orbitals at the bending region of the running low band. Upon introducing the B atoms, p_z orbitals mix with low-energy d orbitals in this region of the BZ and allow the formation of the Dirac cone. Similarly, in the first half of the $\Gamma - K$ line, there

is no running up band that may yield the Dirac cone observed in the diborade lattice, other than the d_{z^2} derived band which is known from the diboride diagram to not mix with any other state. Furthermore, the d_{xz} state is developed from 0.43 eV down to -0.37 eV across that region, contrary to the observation in Figure 2, where it is developed from Γ to K with positive gradient. Such a change in the slope of the band can be ascribed to the presence of the B atom p_z orbitals when they enter the formation of the diboride lattice, which also causes the d_{z^2} and $d_{x^2-y^2}$ orbital derived bands to shift up in energy. This proves that the Zr-B orbitals interplay is crucial in the formation and strength of both Dirac cones, allowing the Zr-B hybridization to locate both Dirac points at the Fermi level, and the electronic delocalization over the complete unit cell.

Applying the symmetry operations of the C_{6v} point group to the iBZ, two dimensional ZrB_2 exhibits 12 inequivalent Dirac cones, which is a remarkable difference with respect to any previously described hexagonal material. This is displayed in the contour line plots of both the valence and conduction band shown in Figure 4, where the same bands of graphene have been included for comparison. Indeed, rotating the iBZ six times to complete the whole BZ of the hexagonal lattice (pointed out by the dashed hexagons), six groups of two Dirac points are reproduced. Note that applying the same operations on the graphene BZ yields three groups of a pair of K and K' points hosting the corresponding cones.

Due to the large size of the Zr atom, SOC is susceptible to introduce some changes in the electronic states. SOC was checked and the resulting band diagram is shown in Figure 5b. meV large band gaps are noticeable at all band crossing, while the rest of the electronic states barely differs from the non-relativistic band structure. It is worth noting that electron-hole pockets are preserved and the band splitting causes a distortion of the Dirac cone in the $\Gamma - K$ line that closes effectively the small gap by overlapping the bands, as shown in detail in the zoom-in inset.

Despite both types of Dirac cones derive from the Zr d-orbitals, the stronger hybridization with the B atoms exhibited by the cone on the $M - \Gamma$ line makes it very sensitive to relative distance variations. External tensile strain expands the lattice and the Zr atom adjusts its vertical distance to the honeycomb lattice, and is able to vanish the Dirac point. Figure 5 shows the evolution of the ZrB_2 electronic states with SOC under increasing tensile strain. The vertical distance to the center of the hexagon is progressively reduced from the original 1.48Å down to 1.44, 1.41, 1.37, and 1.33Å for an enlargement of the hexagonal unit vectors from 1% to 2%, 3% , and 4% respectively. Although the hexagons expand, providing more room to accommodate the Zr atom, the Zr-B bond length is barely modified. The main effect leading to the Dirac cone vanishing can be ascribed to the difference in the p_z - d orbital hybridization as a result of the bonding angle modification. These structural changes, that leave

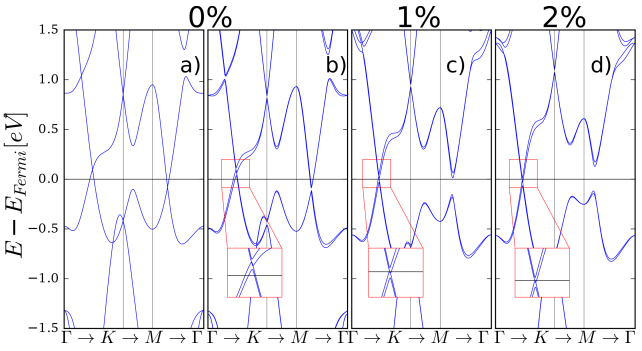

FIG. 5. Non-relativistic band diagram in a) is shown for comparison with the spin-orbit coupling calculation in b). c) and d) shows the evolution of the monolayered ZrB_2 electronic states under tensile strain. Increments are shown in hexagonal lattice parameter percentage. Zr atom vertical position changes as the honeycomb lattice expands, and the Dirac point in the $M - \Gamma$ line vanishes. The superposition of electronic bands upon SOC-induced band splitting prevents from the creation of a gap in the $\Gamma \to K$ line.

the triangular geometry of the Zr atom intact, preserve the Zr-derived Dirac cone in the $\Gamma - K$ line. Although the cone is created with the participation of the B atoms that turn over the slope of the d_{xz} derived band, it is less sensitive to hybridization effects. With no other metallic band to compensate the hole pocket, the Dirac point shifts to exactly the Fermi energy. Similarly, the cone at the K point remains but is shifted in energy.

A distinctive feature of graphene low-energy spectrum is that the Dirac cones at K points are protected by symmetry and from any perturbation that does not violate parity and time reversal symmetries. The metallic character of graphene electronic structure is thus insensitive to deformations such as external stress. On the contrary, the hexagonal network of ZrB_2 is highly sensitive to shear stress which reduces the symmetry of the unit cell and causes the vanishing of either the $\Gamma - K$ or $M - \Gamma$ Dirac points, depending on the direction of the external force. Figure 6a displays the shape of the BZ after symmetry reduction. The modification of the unit cell is realized by modifying one unit cell vector component at a time, as shown in Figure 6b, where the angle between in-plane unit cell vectors is increased. Figure 6c shows the electronic band diagram of ZrB_2 obtained upon applying an external force acting parallel to the x-axis that subtract 0.2 Å to the x-component of the a_y unit cell vector. A Dirac cone in the $\Gamma - M$ line is preserved despite the symmetry reduction, while the Dirac point in the $\Gamma - M'$ line vanishes. Band degeneracy at the K and K' points is also removed. Similarly, decreasing by 0.3 Å the y-component of the a_x vector, a force acting along the y-axis is mimicked. As a result, only the Dirac cone in the $\Gamma - K$ line remains unaffected.

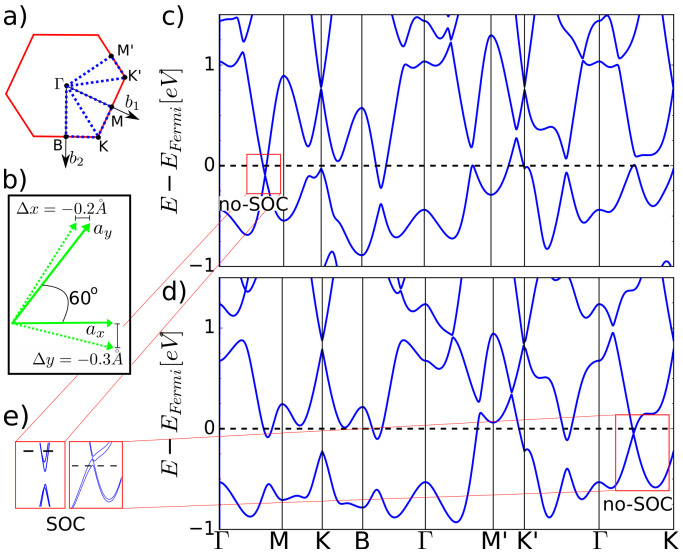

FIG. 6. Dirac cones of monolayered ZrB_2 vanish selectively depending on the applied shear stress direction. a) shows the BZ obtained modifying the unit cell vectors as indicated in b). c) displays the non-relativistic band diagram obtained applying a force along the x-axis that modifies the a_y vector x-component in -0.2 Å. Similarly, d) is obtained modifying the a_x vector y-component in -0.3 Å.

IV. CONCLUSIONS

The existence of twelve inequivalent Dirac cones in the low spectrum diagram of a hexagonal lattice can be realized, without resorting to Rashba SOC or twisted bilayer of triangular lattices[17]. Owing to the formation of monolayered ZrB_2 Dirac cones in the lines joining high symmetry points, the cones are not shared with any neighbouring BZ. The twelve Dirac cones are divided in six groups of two non-symmetry-related cones with a slight electron-pocket compensation. First-principles calculations allowed to unveil the separate contribution of each d-orbital of the transition metal atom, and their hybridization with the B atomic orbitals. A color-scheme enabled to assign the formation of the cones to the Zr d_{xy}, d_{xz}, and d_{yz} orbitals with a contribution from B p_z orbitals as a result of atomic orbital hybridization.

Dirac cones are modified under external physical stimuli differently as a result of the unidentical participation of the B p_z orbitals in the formation of the cones. Owing to the strong Zr-B atoms hybridization, small changes in the bonding angle lead to one cone vanishing. Ignoring SOC, internal symmetry breaking leads to a selective Dirac cone disruption at Fermi level depending on the direction of applied distortion, showing that not all cones are protected by symmetry. SOC induces complete Dirac point vanishing depending on the direction of the external force. These findings suggest that the interplay between d and p orbitals of different atoms, together with the relativistic effect of SOC, creates an environment that offers new avenues to electronics, and may provide a platform that outdoes the capabilities of other 2D materials with Dirac states.

It is worth mentioning that one key issue of monolayered $ZrB2_2$ with a view to its implementation in electronic applications is the robustness of the electronic properties against the disorder introduced by intrinsic or extrinsic defects, such as atomic vacancies and external functional groups. Both short and long range disorder are known to limit the charge transport ability of 2D compounds[25] and, therefore, a systematic analysis of the possible role of defects in an energy-dependent charge mobility framework is proposed for future studies. From our results, where minute network deformations were shown to lead inevitably to drastic changes, the electronic properties of monolayered $ZrB2_2$ can be anticipated as extremely sensitive to network changes. Thus, sensor applications by monitoring electrical changes in the nanostructure upon interaction with foreign species could be expected as a potential technological use of the material. Advanced approaches accounting for the strongly correlated Zr electrons must be considered to study the formation of localized magnetic moments upon composition changes.

V. ACKNOWLEDGMENTS

This work was supported by the U.S. Department of Energy, Office of Science, Basic Energy Sciences, Materials Science and Engineering Division. I acknowledge the computing resources provided on Blues and Fusion, the high-performance computing clusters operated by the Laboratory Computing Resource Center at Argonne National Laboratory. I thank P.B. Littlewood for fruitful discussions and support.

* alejandrolb@gmail.com

[1] K. S. Novoselov, A. K. Geim, S. V. Morozov, D. Jiang, Y. Zhang, S. V. Dubonos, I. V. Grigorieva, and A. A. Firsov, Science **306**, 666 (2004), http://science.sciencemag.org/content/306/5696/666.full.pdf.

[2] P. Vogt, P. De Padova, C. Quaresima, J. Avila, E. Frantzeskakis, M. C. Asensio, A. Resta, B. Ealet, and G. Le Lay, Phys. Rev. Lett. **108**, 155501 (2012).

[3] C. Grazianetti, E. Cinquanta, and A. Molle, 2D Materials **3**, 012001 (2016).

[4] M. E. Dvila, L. Xian, S. Cahangirov, A. Rubio, and G. L. Lay, New Journal of Physics **16**, 095002 (2014).

[5] A. Acun, L. Zhang, P. Bampoulis, M. Farmanbar, A. van Houselt, A. N. Rudenko, M. Lingenfelder, G. Brocks, B. Poelsema, M. I. Katsnelson, and H. J. W. Zandvliet, Journal of Physics: Condensed Matter **27**, 443002 (2015).

[6] F.-f. Zhu, W.-j. Chen, Y. Xu, C.-l. Gao, D.-d. Guan, C.-h. Liu, D. Qian, S.-C. Zhang, and J.-f. Jia, NATURE MATERIALS **14**, 1020+ (2015).

[7] D. Malko, C. Neiss, F. Viñes, and A. Görling, Phys. Rev. Lett. **108**, 086804 (2012).

[8] A. Lopez-Bezanilla and P. B. Littlewood, Phys. Rev. B **93**, 241405 (2016).

[9] K. K. Kim, A. Hsu, X. Jia, S. M. Kim, Y. Shi, M. Dresselhaus, T. Palacios, and J. Kong, ACS Nano **6**, 8583 (2012), pMID: 22970651, http://dx.doi.org/10.1021/nn301675f.

[10] K. Kobayashi and J. Yamauchi, Phys. Rev. B **51**, 17085 (1995).

[11] A. J. Mannix, X.-F. Zhou, B. Kiraly, J. D. Wood, D. Alducin, B. D. Myers, X. Liu, B. L. Fisher, U. Santiago, J. R. Guest, M. J. Yacaman, A. Ponce, A. R. Oganov, M. C. Hersam, and N. P. Guisinger, Science **350**, 1513 (2015), http://science.sciencemag.org/content/350/6267/1513.full.pdf.

[12] B. Feng, J. Zhang, Q. Zhong, W. Li, S. Li, H. Li, P. Cheng, S. Meng, L. Chen, and K. Wu, Nat Chem **8**, 563 (2016).

[13] J. Nagamatsu, N. Nakagawa, T. Muranaka, Y. Zenitani, and J. Akimitsu, NATURE **410**, 63 (2001).

[14] H. T. Hall and L. A. Compton, Inorganic Chemistry **4**, 1213 (1965), http://dx.doi.org/10.1021/ic50030a027.

[15] L. Z. Zhang, Z. F. Wang, S. X. Du, H.-J. Gao, and F. Liu, Phys. Rev. B **90**, 161402 (2014).

[16] N. Matsumi, Y. Chujo, O. Lavastre, and P. H. Dixneuf, Organometallics **20**, 2425 (2001), http://dx.doi.org/10.1021/om010258d.

[17] G. van Miert and C. M. Smith, Phys. Rev. B **93**, 035401 (2016).

[18] G. Kresse and J. Furthmüller, Phys. Rev. B **54**, 11169 (1996).

[19] H. J. Monkhorst and J. D. Pack, Phys. Rev. B **13**, 5188 (1976).

[20] A. Togo and I. Tanaka, Scr. Mater. **108**, 1 (2015).

[21] Elk is an all-electron full-potential linearized augmented plane wave with local orbitals [FP-(L) APW+lo] code, available free of charge at http://elk.sourceforge.net.

[22] V. A. Gasparov, N. S. Sidorov, I. I. Zver'kova, and M. P. Kulakov, Journal of Experimental and Theoretical Physics Letters **73**, 532 (2001).

[23] H. Kinoshita, S. Otani, S. Kamiyama, H. Amano, I. Akasaki, J. Suda, and H. Matsunami, Japanese Journal of Applied Physics **40**, L1280 (2001).

[24] T. G. Gill, A. Fleurence, B. Warner, H. Prüser, R. Friedlein, J. T. Sadowski, C. F. Hirjibehedin, and Y. Yamada-Takamura, 2D Materials **4**, 021015 (2017).

[25] S. Roche, N. Leconte, F. Ortmann, A. Lherbier, D. Soriano, and J.-C. Charlier, Solid State Communications **152**, 1404 (2012), exploring Graphene, Recent Research Advances.